JOURNAL OF GEOPHYSICAL RESEARCH, VOL. 108, NO. C2, 3023, doi:10.1029/2001JC001006, 2003

Wave–current interactions in an idealized tidal estuary

Ray Q. Lin

Department of Seakeeping, David Taylor Model Basin, Carderock Division, Naval Surface Weapons Center (NSWC), West Bethesda, Maryland, USA

Will Perrie

Ocean Sciences Division, Maritime Region, Fisheries and Oceans Canada, Bedford Institute of Oceanography, Dartmouth, Nova Scotia, Canada

Received 6 June 2001; revised 3 July 2002; accepted 6 December 2002; published 8 February 2003.

[1] We extended a recently developed model for wave–current interactions by *Lin and Huang* [1996a, 1996b] to simulate the impact of topography, currents, and slanting coastlines on sea state estimates. Our formulation uses the action conservation equation and the nonlinear dispersion relation, resulting in additional flux terms, $\partial(c_\omega A)/\partial\omega$, $A\partial c_{g\lambda}/\partial\lambda$, $A\partial(c_{g\phi}\cos\phi)/\partial\phi$, and $A\partial c_{g\theta}/\partial\theta$, compared to "standard" wave models such as WAM, where A is spectral action density, c_ω is phase velocity, and $c_{g\lambda}$, $c_{g\phi}$, and $c_{g\theta}$ are group velocities. For large-scale motions in deep water without varying currents, these effects may be neglected. However, for shallow estuary waters with varying currents, we show that these effects can cause as much as 25% variation in wave height estimates during moderate wind conditions. This phenomenon is consistent with observations and theory, for example, regarding isolated topography such as seamounts. *INDEX TERMS:* 4560 Oceanography: Physical: Surface waves and tides (1255); 4556 Oceanography: Physical: Sea level variations; 4255 Oceanography: General: Numerical modeling; *KEYWORDS:* wave–current interactions, time-varying currents and waves, shallow water waves, wave topographic interactions, wave action conservation, nonlinear dispersion

Citation: Lin, R. Q., and W. Perrie, Wave–current interactions in an idealized tidal estuary, *J. Geophys. Res.*, *108*(C2), 3023, doi:10.1029/2001JC001006, 2003.

1. Introduction

[2] For tidal estuaries, such as the St. Lawrence River and Gulf, the problem of forecasting sea state conditions requires consideration of factors such as currents, topography, and slanting fetches. Each of these factors must be carefully modeled in order for the resultant simulation to have some accuracy. For example, the interactions between waves and currents can be quite strong, depending on many factors, such as wave steepness, water depth, the orientation of the waves relative to the currents, etc. In the latter case, cross-stream, upstream, and downstream winds and associated wave fields, interacting with a tidal estuary current, represent three possible wave–current interaction situations. Moreover, sea state is also influenced by the impact of time-dependent currents, topography–swell wave interactions, and the influence of slanting fetch on wave evolution. Wave generation characterized by these factors is quite different from that which may occur in open ocean conditions, where they are absent.

[3] The basic kinematical mechanisms of wave–current interactions have been investigated by *Lin and Huang* [1996a, 1996b]. They showed that nonlinear wave–current interactions must be understood in terms of amplitude and depth dependency in a fully nonlinear dispersion relation, following the studies of *Yuen and Lake* [1982] and *Infeld and Rowlands* [1990]. As suggested by *McLean* [1982], the role of a fully nonlinear dispersion relation is not only in the modulation and propagation of waves, but also in the selection of resonant wave–wave interactions. *Lin and Huang* [1996b] used a fully nonlinear dispersion relation, in conjunction with the action conservation equation, for water of finite depth, to explore the impact of steady and unsteady currents, changing bottom topography and shallow water conditions. They found that these considerations had implications on sea state simulations. While open ocean conditions, with deep water and nonvarying currents, can be simulated by linear dispersion and an energy balance equation, as assumed by the WAM model of *Komen et al.* [1994], *Lin and Huang* [1996b] concluded that fully nonlinear dispersion and the action conservation equation were important for sea state estimation in coastal regions.

[4] In this paper, we extend the formulations of *Lin and Huang* [1996b] to consider factors such as time-varying currents, topography, and slanting wind fields and fetches, typical of a tidal estuary system such as the St. Lawrence River and Gulf. This is done in section 2. In section 3, we discuss numerical schemes suitable for operational wave–current simulations, given these factors. Section 4 presents simulations showing the impact of these factors on sea state estimates in an idealized tidal estuary and for isolated

0148-0227/03/2001JC001006$09.00

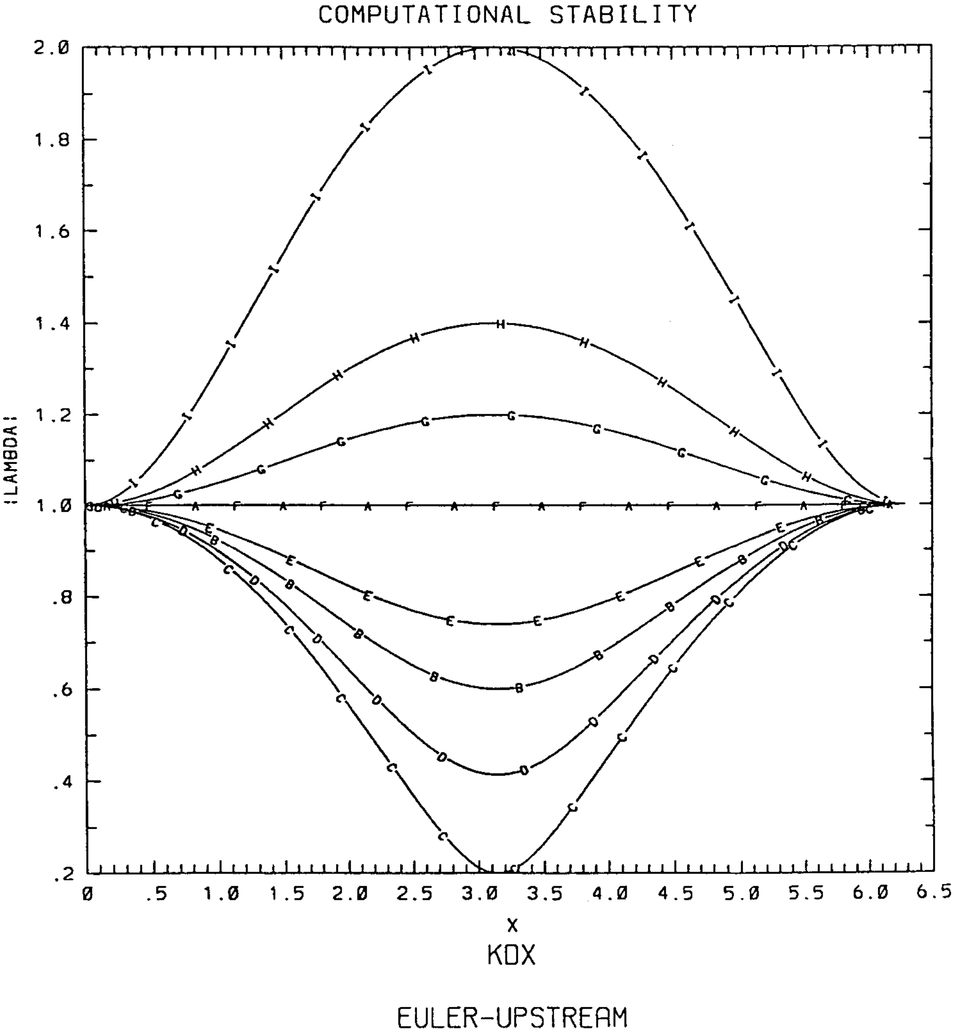

Figure 1. Computational instabilities for the transport equation with (a) first-order Euler scheme, (b) the second-order upstream scheme, and (c), the third-order upwind scheme, where $|\Lambda|$ varies with $k\Delta x$ for different μ: $\mu^B = 0.2$, $\mu^C = 0.4$, $\mu^D = 0.707$, $\mu^E = 0.87$, $\mu^F = 1.$, $\mu^G = 1.1$, $\mu^H = 1.2$, and $\mu^I = 1.5$.

bottom topography. In section 5, we give a discussion of available observational data, and theory in relation to model simulations presented in section 4. Finally, section 6 summarizes our conclusions.

2. Basic Governing Equations

[5] Following the studies of *Whitham* [1974], *Lin and Huang* [1996b], and *Lin* [1998b], the correct nonlinear dispersion relation for wave–current interactions is,

$$\sigma = (gk \tanh kd)^{1/2} \cdot \left[1 + \left(\frac{9\tanh^4 kd - 10\tanh^2 kd + 9}{8\tanh^4 kd}\right)k^2a^2 + \cdots\right]. \quad (1)$$

where σ is the intrinsic frequency in rad s^{-1}, k is the magnitude of the vector wave number $\vec{k}$ in m^{-1}, ak is wave steepness for deep water, g is the gravitational acceleration in m s^{-2}, d is depth in m, and a is the wave amplitude. Equation (1) differs from the usual linear dispersion relation, $\sigma^2 = gk \tanh kd$, in other similar wave models, for example the WAM formulation of *Komen et al.* [1994], by the leading-order $\bigcirc(k^2a^2)$ nonlinear term, which may be large in shallow water. In the former case, k and associated wave crests are not conserved, whereas in latter case, coxnservation of wave crests is a key element in WAM.

[6] Because the full nonlinear dispersion relation of (1) is based on perturbation analysis, its ordering and magnitude are all energy density related. Therefore, to ensure that the increasing energy density does not cause the higher energy terms to overpower the lower-order ones, as water depth decreases, a check is imposed. To guarantee this ordering, we require that waves break when $ak\frac{3\tanh^2 kd+1}{4\tanh^2 kd} \geq 0.3$ in the computations. Wave energy exceeding this limit is set to zero. By comparison, the Stokes limit puts the ak limit very close to unity. This breaking criterion is considered justifiable, in view of laboratory and field observations as reported by *Huang et al.* [1986].

[7] By definition, the intrinsic group velocity is given by $\vec{c}_g = \frac{\partial\sigma}{\partial k}\frac{\vec{k}}{k}$ and the apparent frequency is defined as $\omega = \sigma + \vec{k} \cdot \vec{v}$, where $\vec{v}$ is the ambient current in m s^{-1}. We note that with time-varying tidal currents and finite depth water, not only a, but also d are functions of position

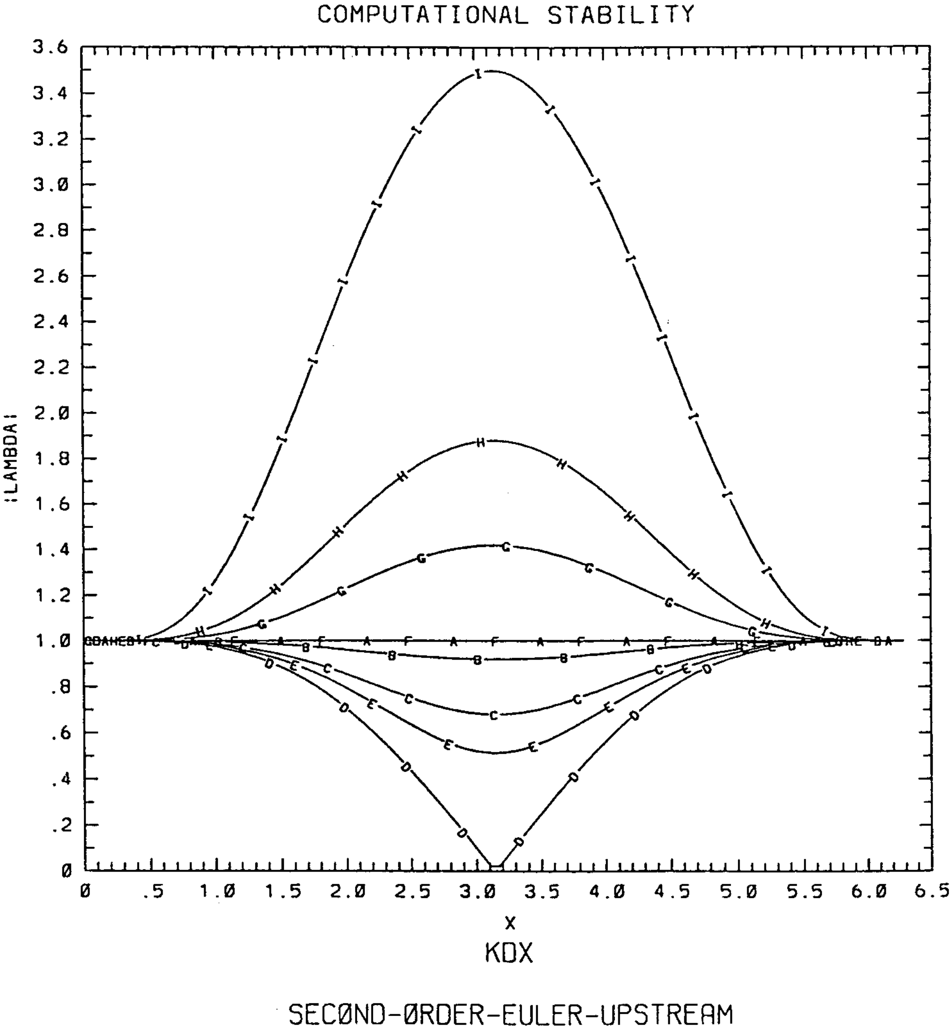

Figure 1. (continued)

and time. Position dependence in a and d in the nonlinear dispersion relation implies that k is not conserved. Although variations in both a and d have been largely neglected by previous modelers, *Whitham* [1974] and *Lin and Huang* [1996b] note that they are important considerations in nonlinear wave kinematics and should be included in simulations of coastal regions, involving time-varying currents and finite depth.

[8] The basic equation for conservation of action density, during wave growth and evolution and during wave–current interactions, is

$$\frac{\partial A}{\partial t}+\frac{\partial\left[\left(c_{g\lambda}+u\right)A\right]}{\partial\lambda}+\cos^{-1}\phi\frac{\partial\left[\left(c_{g\phi}+v\right)A\cos\phi\right]}{\partial\phi}+\frac{\partial[c_\theta A]}{\partial\theta}+\frac{\partial[c_\omega A]}{\partial\omega}=S_{ds}+S_{nl}+S_{in} \quad (2)$$

following the studies of *Whitham* [1974] and *Bretherton and Garrett* [1968]. Here, A is action energy density in units of $\mathrm{m^2\,rad^{-1}\,s^{-2}}$, defined as the energy spectrum N divided by the intrinsic frequency ω, t is time in s, ϕ and λ are latitude and longitude coordinates, and θ is the wave propagation direction, oriented clockwise from north. Source terms, as represented by S_{in} for wind input, S_{ds} for dissipation, and S_{nl} for nonlinear wave–wave interactions, follow the usual WAM formulations. The characteristic propagation velocities are c_θ, c_ω, $c_{g\lambda}$, and $c_{g\phi}$. Equation (2) actually assumes that the dispersion is linear. However, as described by *Lin and Huang* [1996b] and *Lin and Perrie* [1999], the nonlinear dispersion relation in (1) is third order, whereas the nonlinear source function S_{nl} in (2) is fourth order, and it is inconsistent to eliminate the former and retain the latter. Thus, it is important to include the nonlinear dispersion relation. In fact, nonlinear dispersion not only affects the wave–current interactions, but also strongly affects the S_{nl} term. The latter includes both three-wave interactions and four-wave interactions. Quasi-resonant triad interactions may play an important role in shallow water, especially when the long waves are absent. However, triple-product averages of resonant triadic fields will vanish under the assumption of Gaussian statistics, which is often made, and so do not contribute to statistical wave evolution. Moreover, as three-wave interactions may be formulated in terms of reflection terms in modern WAM-type models, they are also not able to transfer energy to lower frequency and growth. Therefore,

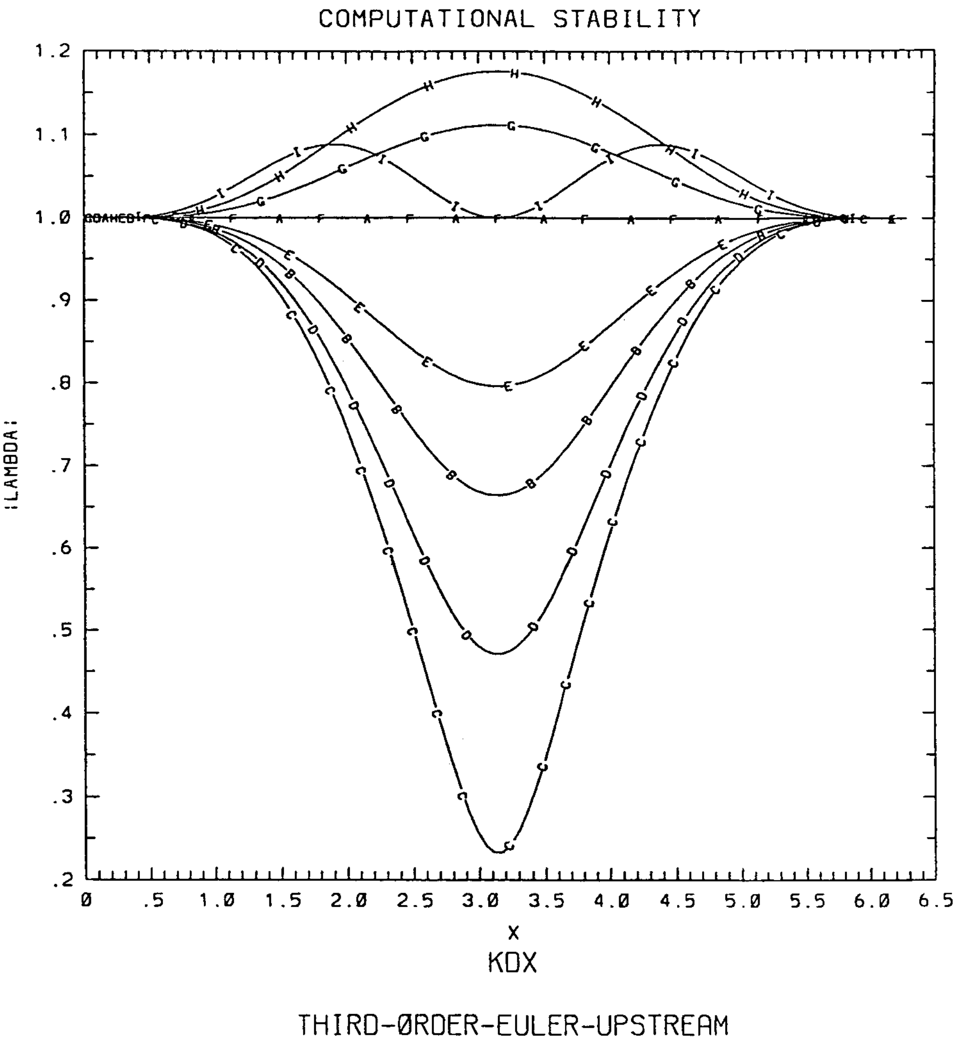

Figure 1. (continued)

triadic interactions cannot play a pivotal role in explaining well-known observations, for example the fact that coastal-trapped waves often have dominant frequencies that are lower than corresponding waves in deep water, with amplitudes greater than corresponding deep water waves.

[9] In order to develop a finite depth global spectrum model, which is suitable to study waves for both deep ocean and shallow water ($kd \geq 0.3$ and $ka \leq 0.3$), we modify the traditional action conservation equation and introduce the weakly nonlinear action conservation equation, as presented in (1) and (2). Because the third-order terms in (1) are not based on the assumption of Gaussian statistics, they are able to transfer the action energy by three-wave interactions in shallow water. Therefore, this action conservation equation should be more accurate than the linear dispersion action conservation equation, particularly for situations such as unsteady currents and depths in shallow water. Moreover, as noted by *Lin and Huang* [1996b], (2) is different from the basic equation implemented by WAM and similar wave models. Although refraction may be included in WAM, the parameterization is different from the wave–current interactions of (2), especially in the coastal region, where water depth and currents can vary rapidly with time. From the study of *Komen et al.* [1994], the balance equation of WAM is,

$$\frac{\partial N}{\partial t} + \frac{\partial\left(c_{g\lambda}N\right)}{\partial\lambda} + \cos^{-1}\phi\frac{\partial\left(c_{g\phi}N\cos\phi\right)}{\partial\phi} + \sigma\frac{\partial\left(c_{\sigma}\frac{N}{\sigma}\right)}{\partial\sigma} + \frac{\partial\left(c_{\theta}N\right)}{\partial\theta} = S_{ds}^{*} + S_{nl}^{*} + S_{in}^{*} + \textit{ refraction}, \qquad (3)$$

where S_{ds}^{*}, S_{ds}^{*}, and S_{in}^{*} are energy source terms corresponding to the action source terms S_{ds}, S_{ds}, and S_{in} in (2). Intrinsic frequency σ is used to avoid wave blocking, whereby two solutions can exist for $|k|$ from the relation $\omega = \sigma + \vec{k}\cdot\vec{v}$, in situations of strong opposing currents, and the energy propagation velocity for certain frequencies may vanish.

[10] Comparing (2) and (3), we note that the WAM invariance of frequency ω implies that $c_{\omega} = \frac{D\theta}{Dt} = 0$. This implies that the term $\partial(c_{\omega}A)/\partial\omega$, which appears in our New Coastal Wave Model (NCWM), in (2), responds very differently from the action density term, $\sigma\frac{\partial\left(c_{\sigma}\frac{N}{\sigma}\right)}{\partial\sigma}$ in the WAM formulation of (3), given unsteady currents and water depths. Moreover, the action flux terms, $A\frac{\partial c_{g\lambda}}{\partial\lambda}$, $A\frac{\partial(c_{g\phi}\cos\phi)}{\partial\phi}$, and $A\frac{\partial c_{g\theta}}{\partial\theta}$, evident in (2), do not include wave amplitude effects in the

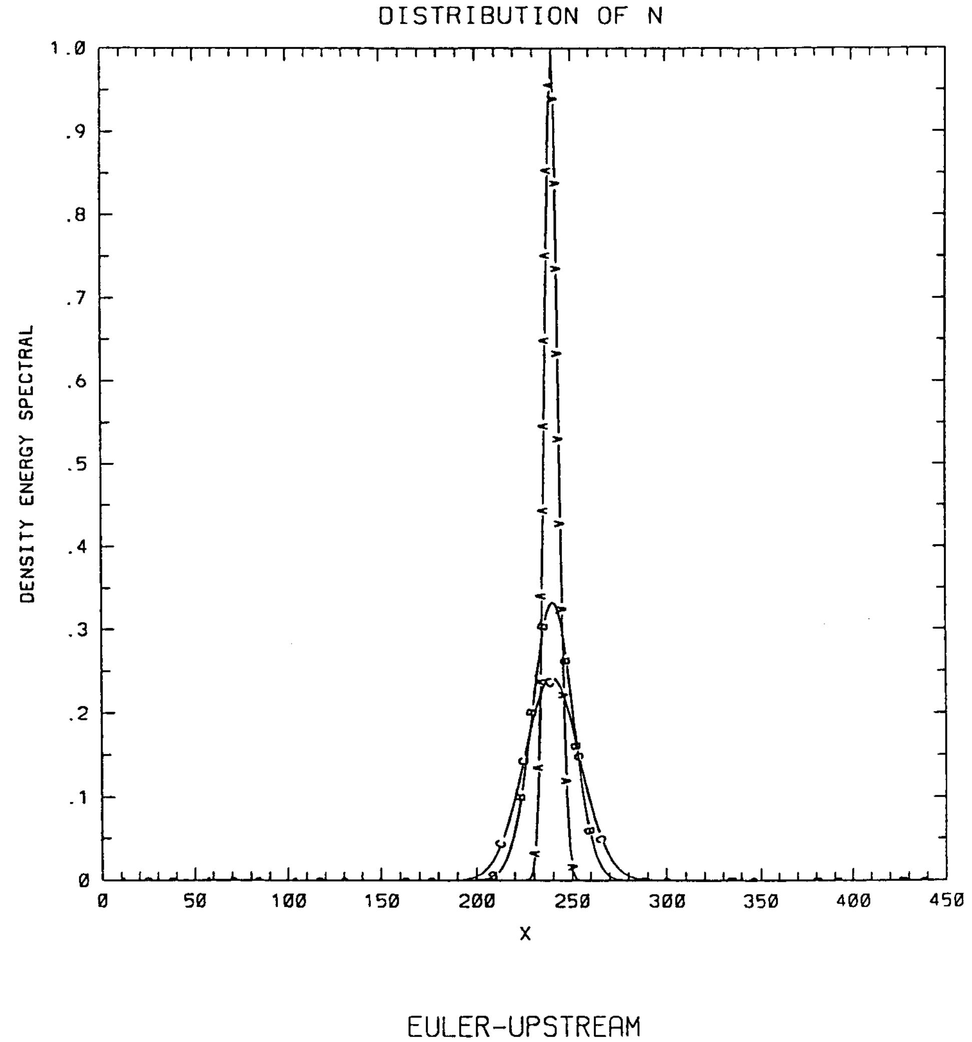

Figure 2. As in Figure 1, showing a simple test for numerical dissipation and dispersion.

WAM formulation, and in fact vanish in steady situations. These "extra" action flux terms are retained in the NCWM formulation in unsteady situations because of nonlinear dispersion, which implies that wave crests are not conserved. For large-scale motions, in deep water, the contributions of these flux terms may be neglected, as a function of time, whereas for small-scale tidal estuary motions, these contributions become important. For example, relatively narrow shallow regions of an estuary can have long fetches, in directions along the estuary. In these situations, wave–current interactions are important, especially under high wind conditions.

[11] In deep water, (3) implies that energy is invariant following a wave, when the source terms are set to zero. However, in coastal waters, although parameterized refraction terms allow the occurrence of energy shifts [see *Günther et al.*, 1993], parameterizations cannot account for all possible wave–current interactions. For example, *Lin and Huang* [1996b] note that under steady current conditions, variations in depth should cause changes in N. However, (3) cannot satisfy the simple analytic relation Nc_g = *constant* derived by *Phillips* [1977], for waves propagating toward a beach with no currents. Therefore, in coastal regions, with currents and changing topography, c_g and σ become functions of position, WAM-type models should give substantially different results compared to models such as NCWM, based on (2).

[12] To consider the implications of topography, finite depth, time-dependent currents and nonlinear dispersion, we must consider the characteristic propagation velocities c_θ, c_ω,$c_{g\lambda}$, and $c_{g\phi}$. A full discussion of these terms is given by *Lin and Huang* [1996b] and *Lin* [1998b]. The group velocities in the longitudinal and latitudinal directions, $c_{g\lambda}$ and $c_{g\phi}$ may be represented as

$$
\begin{aligned}
c_{g\lambda} &= \frac{c_g \sin\theta + u}{R\cos\phi}, \\
c_{g\phi} &= \frac{c_g \cos\theta + v}{R}
\end{aligned}
\tag{4}
$$

where R is the Earth's radius. These expressions are found in both NCWM and WAM, as well as other standard modern wave models. Formulations for $c_\theta = \frac{D\theta}{Dt}$ and $c_\omega = \frac{D\omega}{Dt}$ are

$$
\begin{aligned}
c_\theta &= \frac{D\theta}{Dt} = \frac{1}{k}\frac{\partial\sigma}{\partial d}\frac{\partial d}{\partial n} + \frac{1}{k}\left(c_g - c\right)\frac{\partial k}{\partial n} + \frac{\vec{k}}{k}\cdot\frac{\partial\vec{v}}{\partial n}, \\
c_\omega &= \frac{D\omega}{Dt} = \frac{\partial\sigma}{\partial d}\frac{\partial d}{\partial t} + \vec{k}\cdot\frac{\partial\vec{v}}{\partial t} + \vec{v}\cdot\frac{\partial\vec{k}}{\partial t} + \left(\vec{v}+\vec{c}_g\right)\cdot\nabla\left(\sigma + \vec{k}\cdot\vec{v}\right),
\end{aligned}
\tag{5}
$$

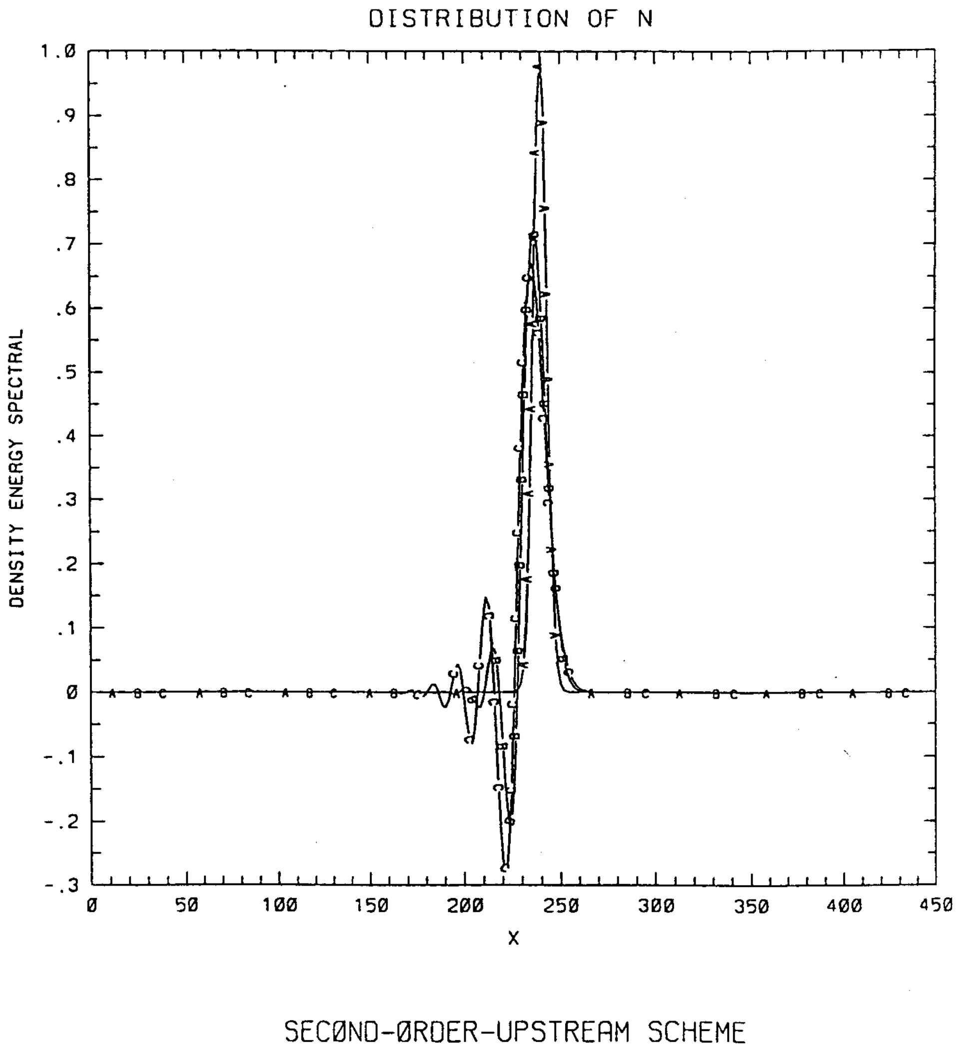

Figure 2. (continued)

following the nonlinear dispersion relation in (1), where n is in the direction of vector $\vec{k}$, c is phase velocity, and $\vec{v}$ is the current velocity. These c_θ, c_ω are implemented in NCWM.

[13] These c_θ, c_ω expressions differ significantly from those implemented in standard linear dispersion wave models such as WAM. In the latter case, c_θ and c_ω are given by

$$
\begin{aligned}
c_\theta &= \frac{1}{k}\frac{\partial\sigma}{\partial d}\frac{\partial d}{\partial n} + \frac{\vec{k}}{k}\cdot\frac{\partial\vec{v}}{\partial n}, \\
c_\omega &= 0.
\end{aligned} \tag{6}
$$

The c_θ and c_ω formulations of WAM are acceptable only if the normalized wave steepness, $\epsilon = ak\frac{3+\tanh^2 kd}{4\tanh^3 kd}$, is very small, as discussed by *Lin and Perrie* [1999]. However, in shallow water coastal regions, although the wave steepness ak may be very small, the normalized wave steepness $\epsilon = ak\frac{3+\tanh^2 kd}{4\tanh^3 kd}$ may be very large. Under these conditions, wave–current interactions will be underestimated by WAM. Moreover, because WAM implicitly requires $c_\omega = 0$, it cannot simulate the wave–current interactions effected by water depth and frequency variation, nor can it simulate the flux terms, $\partial(c_\omega A)/\partial\omega$, $A\frac{\partial c_{g\lambda}}{\partial\lambda}$, $A\frac{\partial(c_{g\phi}\cos\phi)}{\partial\phi}$, and $A\frac{\partial c_{g\theta}}{\partial\theta}$.

[14] Having established the analytic expressions for the kinematics, we present numerical wave–current interaction tests in the following sections. These tests show the difference between our NCWM formulation, based on the full nonlinear dispersion relation and the linear approximations used in the WAM formulation. Of course, we cannot totally exclude the influences of the different numerical schemes and different types of model equations in these comparisons. WAM uses the energy transport equation, whereas NCWM uses the action conservation equation.

3. Numerical Method

[15] To develop an accurate wave model, one needs accurate physical source terms, as well as a numerical method, with minimum dissipation and dispersion. This section is concerned with possible numerical methods that may be implemented to evaluate the physical source terms.

3.1. Euler Scheme

[16] WAM uses the classical Euler scheme, which has considerable numerical dissipation and dispersion. A comparison between the first-order Euler scheme, as imple-

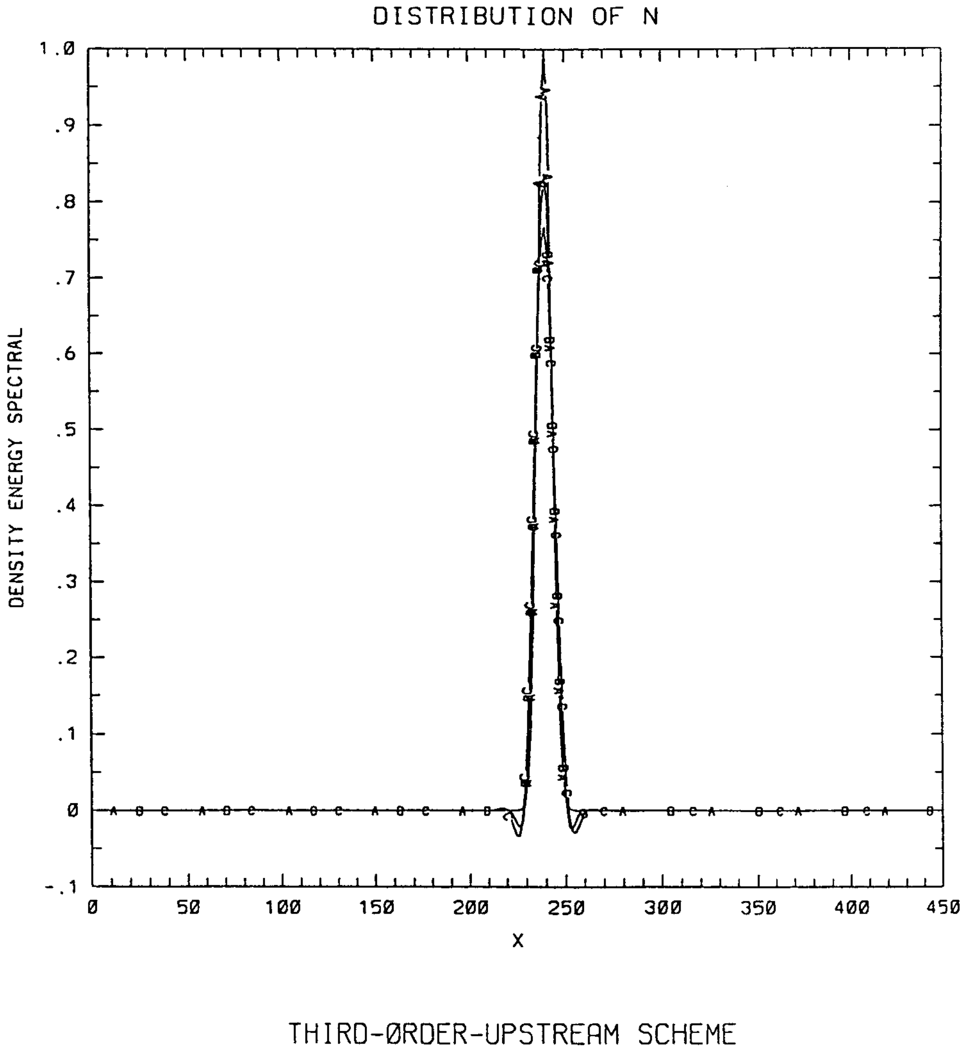

Figure 2. (continued)

mented in WAM, with higher-order Euler schemes, in terms of numerical dispersion and dissipation and computational instability, is discussed in this section.

[17] The classic Euler scheme converts a differential equation to difference format, for example, the spatial and temporal differences of the energy balance equation (3) in Cartesian coordinates, is

$$\frac{N_j^{n+1} - N_j^n}{\Delta t} = \left(c_g + u_j\right)\frac{N_{j-1}^n - N_j^n}{\Delta x}$$

where n is the number of the time step and j is the number of the grid point. To investigate dispersion, dissipation and instability, we assume $N_j = N_0 \exp[ik(j\Delta x - v_j t)]$, where N_0 is the boundary value at $x = 0$, k is the wave number in space and $v_j = (c_g + u)_j$. This implies,

$$|\Lambda|_j = \frac{N_j^{j+1}}{N_j^n} = 1 + \mu_j(\cos k\Delta x - 1) - i\mu_j \sin k\Delta x$$

which is an analytic relation for the computational stability parameter $|\Lambda|$ expressed in terms of $k\Delta x$ and μ_j. Figure 1 shows the computational instability for the transport relation of (2) as implemented in WAM, using the (1) first-order Euler scheme, (2) the second-order upstream scheme (second-order Euler), and (3) the third-order upstream. The results show that the first-order Euler scheme, as well as corresponding higher-order schemes, are all conditionally computationally stable schemes, for the transport relation of (2).

[18] To study numerical dissipation and dispersion, we will use a simple test as shown in Figure 2. The initial spectral energy density function is given by $N^{(0)} = \exp\{-k[x - (c_g + u)t_o]^2\}$, where $k = 0.2$, $t_o = 10$, $(c_g + u) = c_1 + c_2[1 = \cos(j\Delta x)]$, $c_1 = 0.6$, $c_2 = 0.2$ and $\Delta x = 0.5$. Figure 2 gives (1) line A, which is the true solution, (2) line B, the numerical solution for $\Delta t = 0.25$, and $n = 400$ time steps, and (3) line C, the numerical solution for $\Delta t = 0.5$ and $n = 200$. Our analysis leads us to following general conclusions:

1. Simply increasing the order of a numerical scheme will not yield better solutions.

2. Although higher-order schemes decrease numerical errors, numerical dissipation and dispersion continue to be excited, for any finite order.

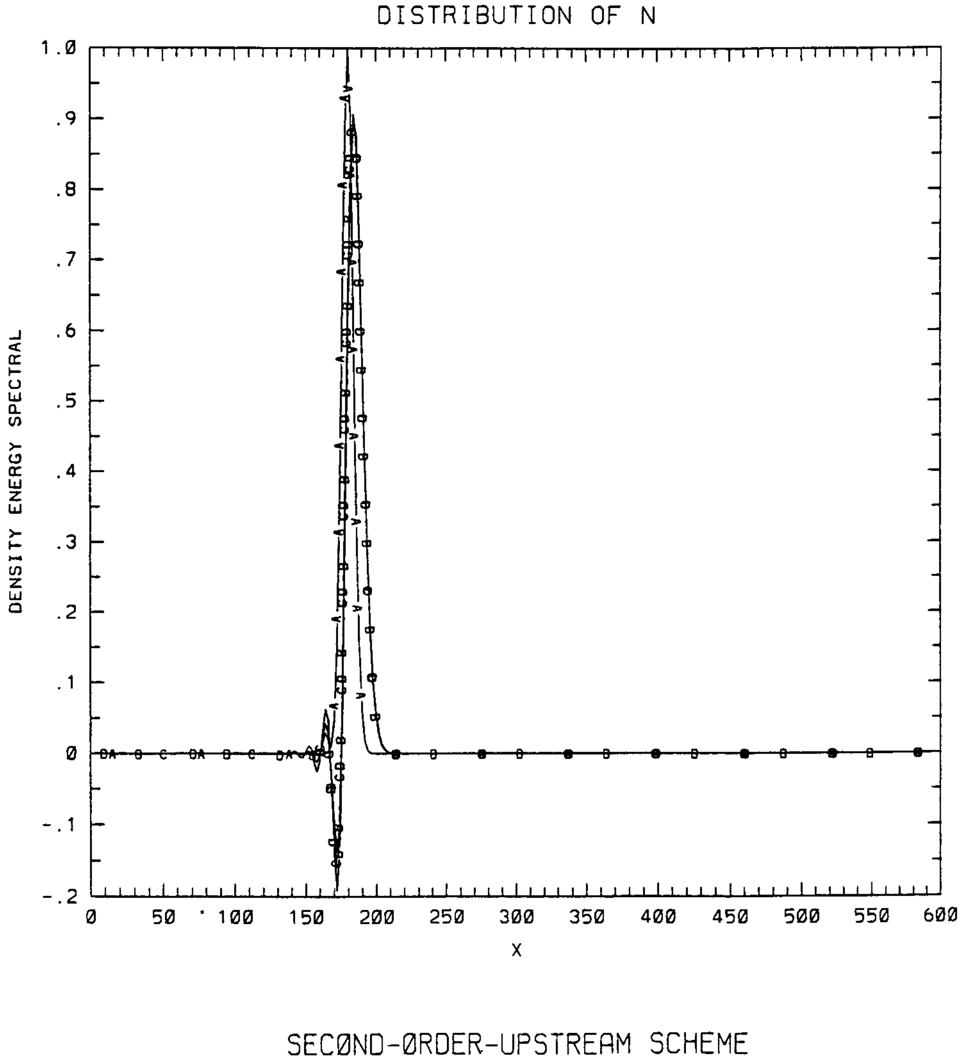

Figure 3. A simple test for computational instability, numerical dissipation, and dispersion for the transport equation, when the time step is 1/10 that of Figure 2 using (a) the second-order upwind scheme, (b) the third-order upwind scheme, and (c) the ICN scheme (with $\alpha = 0.$).

3. Dissipation dominates when m is odd and dispersion dominates when m is even, where m is the order of the higher-order scheme, $m = 1, 2, 3\ldots$

4. When m increases beyond 2, the boundary conditions become increasingly more complicated.

5. The key to limiting numerical errors, in any order of Euler upwind scheme, is to use very small Δt. Unfortunately this requires enormous amounts of computer time.

[19] For studies devoted to wave–current interactions, there is another more serious shortcoming to the Euler upwind schemes. We are required to deal with problems that have finite spectral bandwidth. Finite bandwidth implies that dissipation and dispersion will be *nonuniform* for different wave components. Such effects cannot be separated from other real physical processes, for example wind input, S_{in}, dissipation, S_{ds} and wave–wave interactions, S_{nl}, which are wave number and frequency dependent.

3.2. Action Conservation Equation Scheme

[20] As presented in section 2, a proper description of wave–current interactions involves the action conservation equation. Computational instability for the transport equation is entirely different from that of the conservation equation, because numerical schemes can be conditionally stable in the former case, while being unconditionally unstable in the latter case. To demonstrate this computational instability difference, we consider the numerical schemes: (1) second-order upstream, (2) third-order upstream, and (3) ICN scheme, which is the iterative approximation of the Crank–Nicholson scheme considered by *Lin and Huang* [1996a]. Results are presented in Figures 3 and 4. We reduce the time step by 1/10, compared to the time step in Figure 2, and reobtain the results shown there for the transport equation, in Figure 3. Corresponding results for the conservation equation are shown in Figure 4.

[21] Comparing Figure 4 with Figure 3, we see that the same numerical schemes are stable for the transport equation, but unstable for the conservation equation. The time step of the numerical solutions in Figure 4 is also 1/10 that of Figure 2. In fact, no matter how small we make the time step in Figure 4, the solutions are

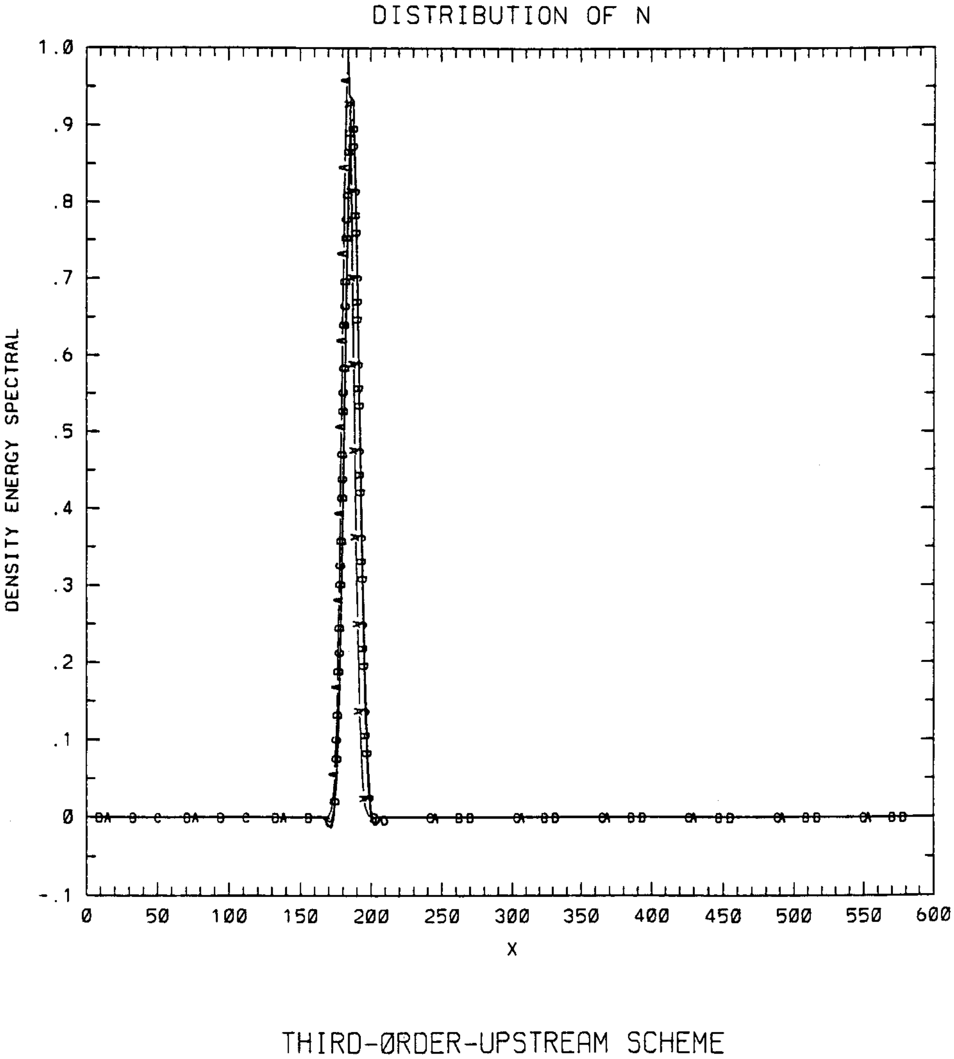

Figure 3. (continued)

always unstable because these numerical schemes are unconditionally unstable for the conservation equation. Therefore, we must use other methods to treat this equation.

[22] *Lin and Huang* [1996a] and *Lin* [1998a] proposed a second-order semi-implicit (SOSI) scheme with a directional filter for the action conservation equation. Although dispersion does not generate instability or an oscillatory tail for large timescales in the SOSI scheme, without the directional filter, action is spread around the propagation direction and the total action increases. However, nonconservation of action is a classical difficulty encountered in numerical solutions of hyperbolic conservation equations. To compensate for this property, *Lin and Huang* [1996a] apply a directional filter, which achieves conservation of action and uses a weighting function to suppress numerical dispersion.

[23] An alternate somewhat simpler scheme consists of the third-order Runge–Kutta scheme. The accuracy of the latter scheme may be only slightly lower than that of the filtered SOSI scheme. The CPU time for a third-order Runge–Kutta scheme maybe only slightly greater. Finally, the third-order Runge–Kutta scheme is both computationally stable and easy to use. If (2) can be simplified as,

$$\frac{\partial A}{\partial t} = F\left(A, \vec{k}, x, y, t, d\right),$$

where $F(A,\ \vec{k},\ x,\ y,\ t,\ d)$ represents flux terms, then

$$\begin{aligned} y_1 &= (dt/2)F\left(A^{(n)}, \vec{k}, x, y, t, d\right); \\ y_2 &= (3dt/4)F\left(y_1, \vec{k}, x, y, t, d\right); \\ A^{(n+1)} &= (dt/9)\left[2F\left(A^{(n)}, \vec{k}, x, y, t, d\right) + 3F\left(y_1, \vec{k}, x, y, t, d\right)\right. \\ &\quad \left. + 4F\left(y_2, \vec{k}, x, y, t, d\right)\right] \end{aligned} \tag{7}$$

represents the third-order Runge–Kutta method. This method is adopted for the results shown in this study.

4. Tests With an Idealized Tidal Estuary

[24] This section presents model results, for NCWM and WAM, for a tidal estuary which is qualitatively similar to

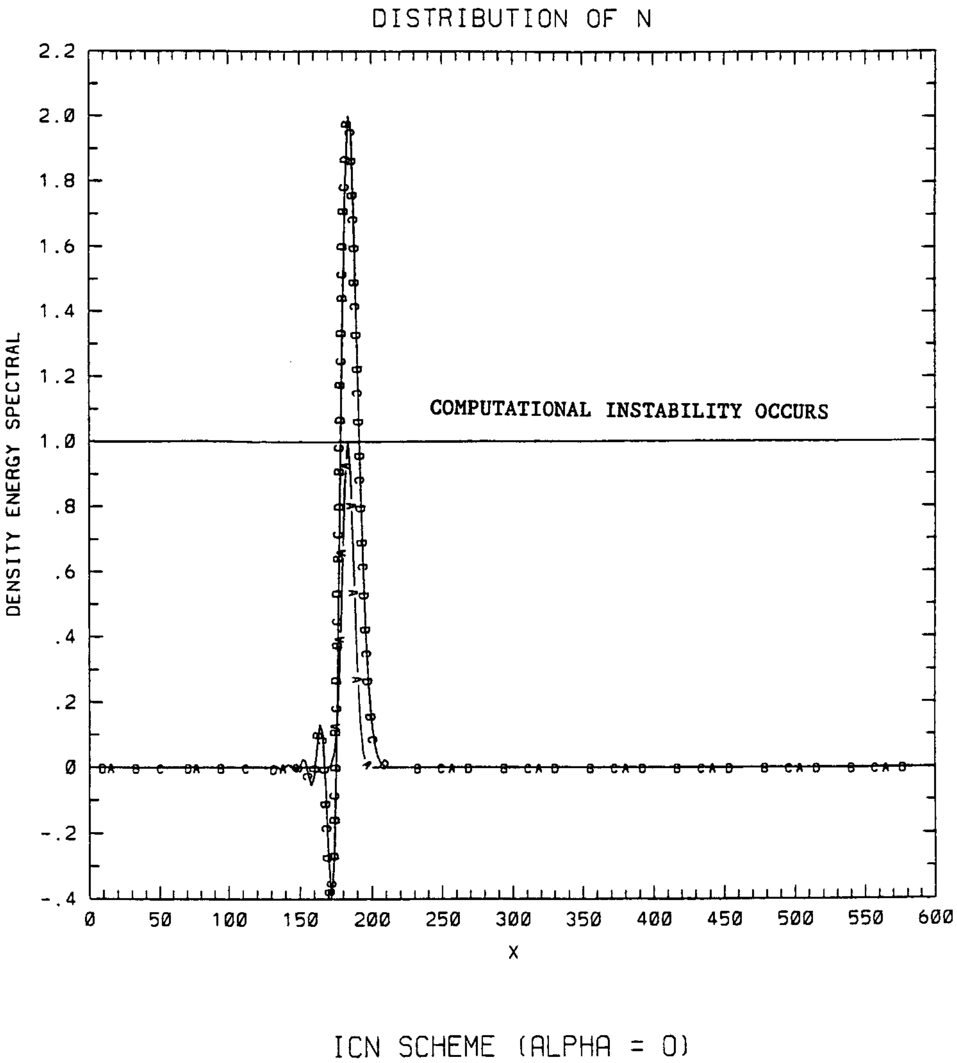

Figure 3. (continued)

the St. Lawrence River and Gulf. Assumed estuary effects include wave–current interactions, the effect of currents and also finite time-varying water depth. A constant wind speed of 17 m s^{-1} at 10 m reference height is assumed, representing rather high wind conditions. Calculations for the nonlinear wave–wave interactions, S_{nl}, in present formulations for both WAM and NCWM, are inaccurate because they are based on DIA (the discrete interaction approximation). These inaccuracies are discussed by *Lin and Perrie* [1999]. Inaccuracies in S_{nl} imply inaccuracies in the resultant two-dimensional energy spectrum, $E(f, \theta)$. However, because both models incorporate tuning to one-dimensional energy–fetch curves, as measured by field experiments such as JONSWAP [*Hasselmann et al.*, 1973], some of this inaccuracy is removed and it is reasonable to present contours of the significant wave height H_s. Detailed discussion of the effects of current shears and bottom slopes on the wave spectrum, for example energy refraction through focusing and defocusing, is given by *Lin and Huang* [1996b]. For all tests given here, the spectra are discretized by 25 frequencies from 0.04177 to 0.41145 Hz and 24 angles at 15° width.

[25] We assume the estuary is oriented along the x-coordinate axis from upstream (x = 0) to downstream (x = 1000 km). In these tests, the space discretization is 5 km and the time step is 5 s. The width of the estuary is 20 km at the upstream "end" of the grid and 100 km at the downstream "end" at the estuary mouth. The estuary width is assumed to linearly increase from upstream to downstream. The water depth is assumed to increase exponentially from upstream to downstream, following the relation,

$$d(i) = -3e^{\left(i-10^3 km\right)^2}/2.94 \times 10^3, \tag{8}$$

where i represents the grid index along the x axis. For simplicity, the tidal current is assumed to satisfy the form $0.4\sin(2\pi t/T)$, where t is time, and T is the tidal period, which is set to 24 hours for this study. The current component due to the gravity, from upstream to downstream, is assumed to have a maximum of 1 m s^{-1}, which decreases the further one moves downstream, because not only does the cross section of the estuary increase but the depth also increases. Figure 5 shows the total current as a

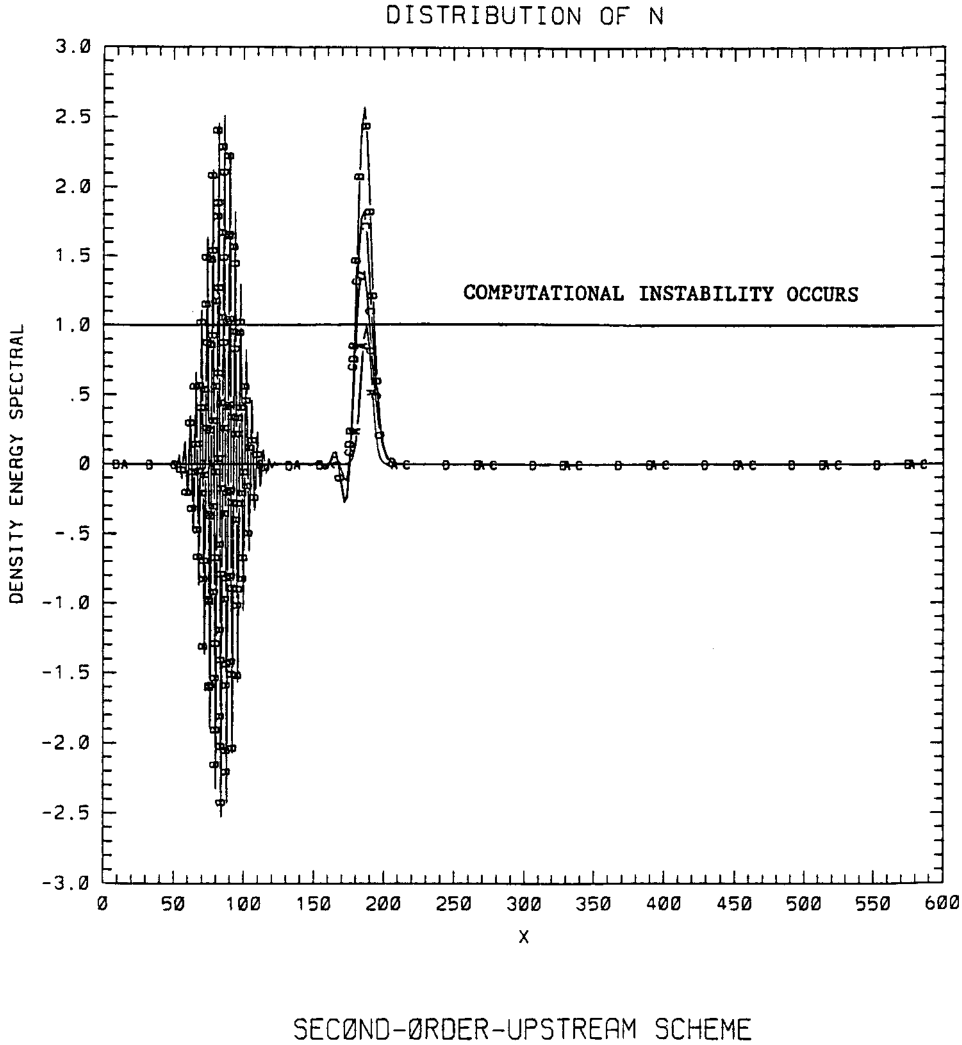

Figure 4. As in Figure 3 for the conservation equation.

function of time. In actuality, both the tidal current and the gravity-forced current components are proportional to the bottom steepness.

4.1. Cross-Stream Winds

[26] In this test we assume cross-stream winds. The wind blows constantly along the y axis, perpendicular to the x axis along which the estuary is oriented. Figure 6 shows the significant wave height H_s distribution at 6 hourly intervals. A 24 hour period was used to warm up the model, prior to achieving these results. In this case, the water depth is assumed finite, following equation (30) with no irregularities, seamounts or "bumps." The H_s contours in Figure 6a are at intervals of 1 m. As fetch increases, H_s increases along the wind direction, as in all operational wave models. The maximum H_s is experienced near the north end of the estuary mouth, because that is where the estuary is widest and the waves have the longest fetch, for cross-stream winds. Figure 6a also shows that for NCWM, H_s oscillates periodically in time, along the x axis, which is the direction of the current. Corresponding results from the WAM model, as shown in Figure 6b, achieve a maximum H_s of 6.1 m, with no oscillation.

[27] The most interesting phenomenon presented in Figures 6a and 6b is the oscillatory H_s exhibited by NCWM. Clearly, a simulation of the H_s cycle and related wave spectrum $E(f, \theta)$ is essential for estimating and predicting H_s on the estuary. The H_s cycle is related to the tidal current and water depth variability. It is composed of a daily movement in the direction along which the current flows, as well as a periodic oscillation in time. These overall characteristics would still occur for somewhat different bottom slopes, or current shears. However, besides not having an H_s cycle, WAM differs from NCWM in having strong numerical dissipation, assuming linear dispersion and indirectly calculates wave–current interactions using parameterizations for refraction and reflection.

4.2. Downstream Winds

[28] Figures 7a and 7b are the same as Figures 6a and 6b, except the wind is blowing along the river length from upstream to downstream direction. In this case, the maximum H_s appears in the downstream region. However, due to the wave–current interactions, and also the effects of bottom slopes and current shears, the maximum H_s does not always occur in the most extreme downstream region of the

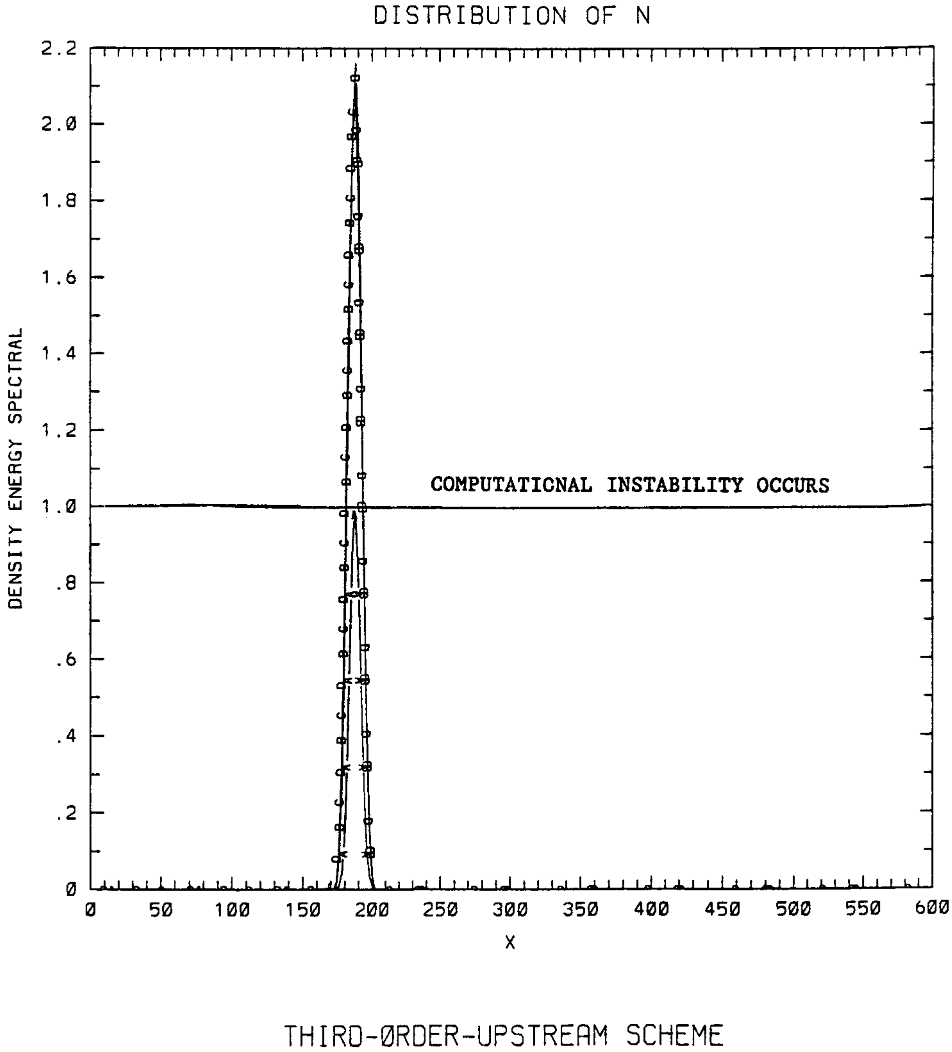

Figure 4. (continued)

grid. As simulated by NCWM, the maximum H_s oscillates in space and time, with a variation of about 2 m. The 4 m isoline is indicated in Figures 7a and 7b. Corresponding WAM results are presented in Figure 8b, showing no H_s cycle.

4.3. Upstream Winds

[29] Figures 8a and 8b are the same as Figures 7a and 7b, except the wind is blowing along the river from downstream to upstream. In this case, the maximum H_s is located near the upstream region of the grid (in the downwind direction). However, as in Figure 7a, NCWM simulation simply that the maximum H_s does not always occur in the extreme upstream portion of the grid, exhibiting an H_s cycle in space and time, because of wave–current interactions. Corresponding WAM results are presented in Figure 8b, showing no H_s cycle.

4.4. Finite Water Depth Effects

[30] Finally, we consider the effect of topography on swell wave propagation, following the studies of *Haidvogel and Beckmann* [1999], *Lin and Huang* [1996b], and *Pedlosky* [1979]. In this test, we assume there is no wind. For topography, we assume the river is uniformly 100 km wide and 300 m deep, with a seamount or "bump" which is 12 km wide, 200 m high, and 100 m below the sea surface, near the estuary mouth, as shown in Figure 9a. The assumed tidal current is periodic, as discussed in section 3. The right side of Figure 9a is assumed downstream and the left side is upstream. There are many theories about tidal current interactions over isolated topographic features and their ability to generate seamount-trapped waves [*Brink*, 1995; *Chapman*, 1988; *Chapman and Haivogel*, 1993]. In general, the strength of the seamount-trapped waves depends on the Burger number, $B = Nh/f_C W$, where N is the buoyancy force, W is the width of the seamount, h is the seamount height, and f_C, the Coriolis force. Seamount-trapped waves, like all internal waves, decrease in amplitude as their distance to the sea surface decreases. The rate of decrease depends on buoyancy forcing. Usually a second maximum in the seamount-trapped wave amplitudes appears at the thermocline.

[31] NCWM simulations, shown in Figure 9b, imply that maximum significant wave height H_s oscillations occur on top of the seamount. These are called "seamount-trapped waves." The "bottom-forced" H_s cycle in Figure 9b has a variation of about 2 m, over the time period of the tidal

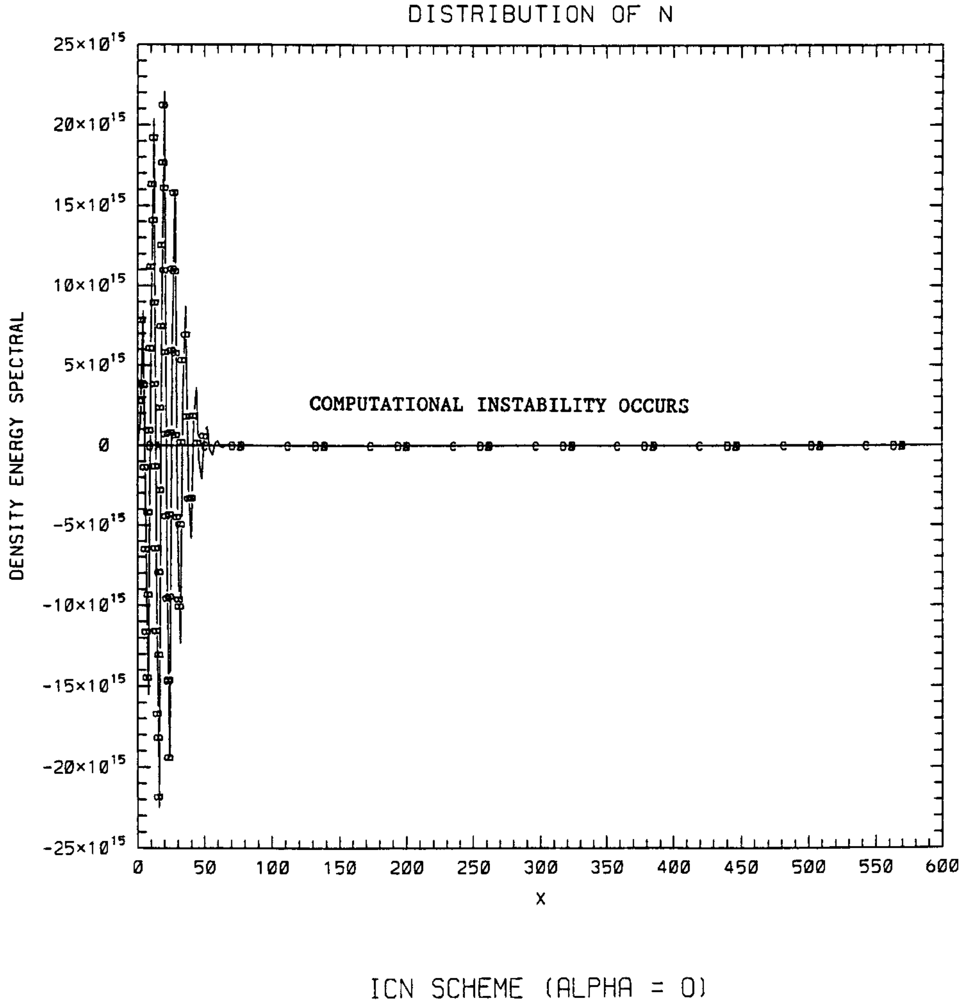

Figure 4. (continued)

cycle. The magnitude of the H_s cycle depends on the free wave frequency, which depends on the Burger number, *B*. The tongue of high wave height water along the "top" occurs because the waves propagate from the western edge of Figure 9b and the seamount-trapped wave effect does not reach the northeast and northern regions of the plot. If the free wave frequency is close to the forcing frequency, then resonance can occur. The H_s contours of Figure 9b result from the action conservation and nonlinear dispersion effects, as typified by action flux terms that appear in the NCWM formulation. These terms do not appear in the WAM formulation. Although these terms are not important for large-scale motions and deep water, they become important for small-scale motions, in shallow tidal estuary water. Corresponding results for WAM are given in Figure 9c. This shows no swell contours, indicating that the swell waves in WAM do not feel the bottom and simply propagate over the seamount.

5. Discussion

[32] The current–depth–wave interactions above the seamount, in the NCWM formulation, result in the dipole wave height structures shown in Figure 9b. This is related to observed experimental phenomenon, specifically the tidal and low frequency currents and associated dipole characteristics over the top of the Fieberling Guyot, located in the North Pacific ocean (32.5°N, 127.75°W). Fieberling Guyot has a 4500 m height and 40 km base width in 5000 m depth water. Its top is 500 m below the sea surface, as shown by *Beckmann and Haidvogel* [1997, Figures 1 and 2]. Figure 9d is adapted from the study of *Beckmann and Haidvogel* [1997, Figure 7] and gives a snapshot of the density perturbation at 500 m depth, with mooring sites of *Brink* [1995] indicated by solid circles. As presented by *Beckmann and Haidvogel* [1997], the dipole current structures indicate a first azimuthal mode seamount-trapped wave [*Brink*, 1989]. This is the response to barotropic tidal forcing and is well known from previous idealized studies of flow around idealized seamounts [*Brink*, 1990; *Haidvogel et al.*, 1993]. The estimated wave amplitude, corresponding to the maximum velocity, exceeds 17 cm s^{-1}, which is in close agreement with the O(20 cm s^{-1}) observed value [*Brink*, 1995]. Because seamount-trapped waves are bottom-trapped waves, their amplitudes decrease as distance to the surface decreases, as noted above. However, this decrease is nonlinear and usually a second amplitude maximum appears in the thermocline near the sea surface

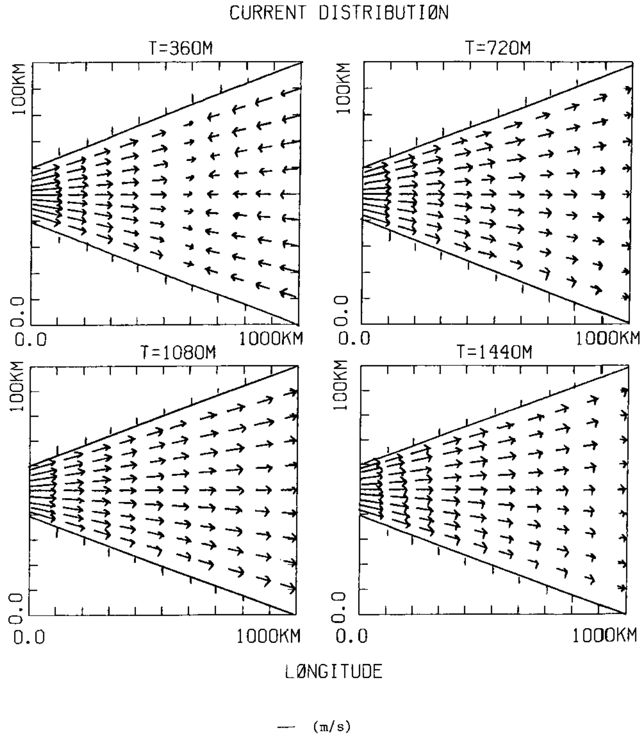

Figure 5. Current in the estuary as a function of time.

because of dependence on rapid changes in the temperature and density with depth. If a surface wave can reach the thermocline, then the internal waves can transfer their energy to surface gravity waves through wave–current interactions. This was recently shown theoretically by R. Q. Lin and S. Chubb (A study of seamount trapped wave in northwest Pacific Ocean by comparison the radar images and model results, submitted to *Journal of Geophysical Research*, 2001, hereinafter referred to as Lin and Chubb, submitted manuscript, 2001). Thus, in this case, the dipole current structures of *Beckmann and Haidvogel* [1997] can then be intensified at sea surface to the extent that they can be observed.

[33] Another seamount example consists of two seamounts in the northwest Pacific ocean, near 51°N and 164°E. These are small seamounts, with heights of only about 0.7 km on base diameters of about 20 km width, in an ocean depth of 5 km. However, the trapped waves on top of these seamounts are significant enough, through wave–current interactions that transfer their energy to the waves on the sea surface, that features of their structure are captured by SAR radar images of *Etkin et al.* [1991], as shown in Figure 9e. Because the image was synthesized from data collected by Satellite "Cosmos-1870" using optical rather than digital techniques, it is impossible to quantitatively extract the associated surface wave spectrum [*Hasselmann et al.*, 1985; *Krogstad et al.*, 1994; *Dowd et al.*, 2001]. However, within limits, relative variations within the image are notable. Specifically, two prominent features are clearly visible, directly above the locations of the two seamounts, as noted by *Chelomei et al.* [1990]. The intensity variations in the center of the image, associated with darkened oval-like structures, and brightened, undulating, horizontal streaks, occur in the regions where one expects "leeward waves" between the two underwater seamounts. Therefore, even very small seamounts can result in significant sea surface features, if the thermocline is sufficiently distinct with waves that are long enough to reach the thermocline and if wave–current interactions are strong. Without wave–current interactions, even with a very strong

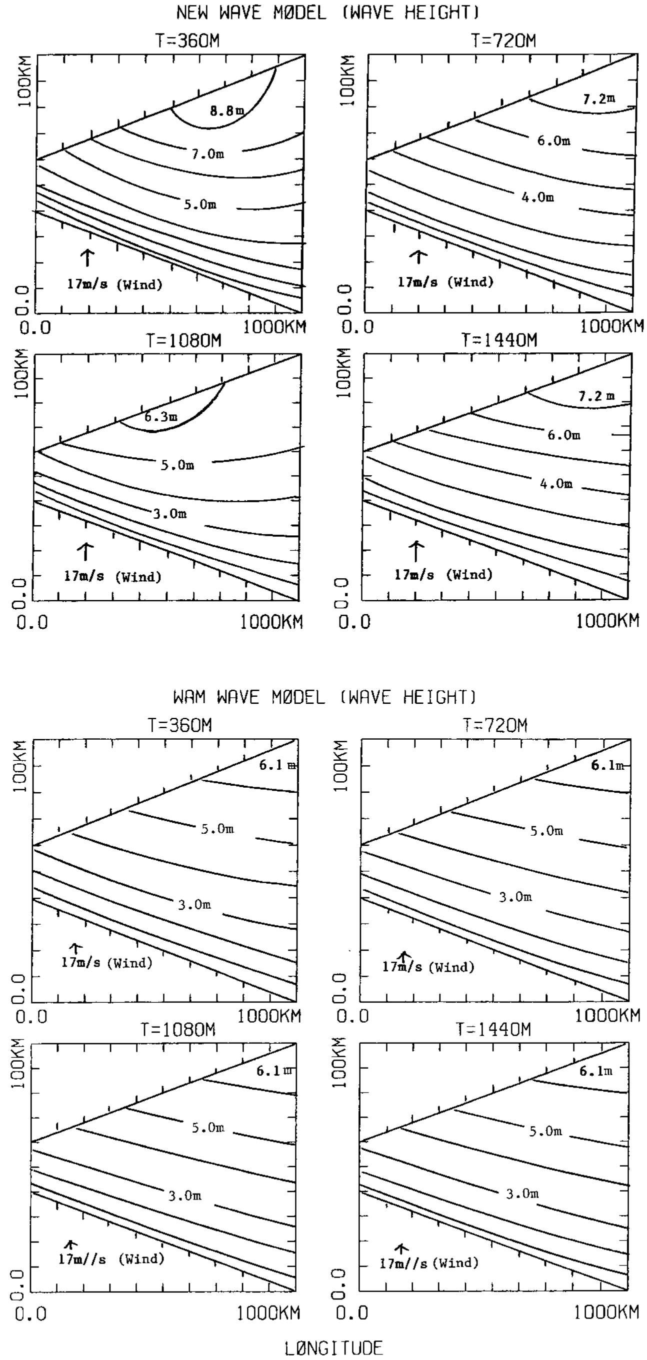

Figure 6. Significant wave height H_s distribution for idealized St. Lawrence River, with smooth bottom topography and wind speed 17 m s^{-1} oriented perpendicular to the central axis of the river and with an assumed tidal current of 0.4 m s^{-1} with a 24 hour period: (a) from NCWM and (b) from WAM model. Units are in m.

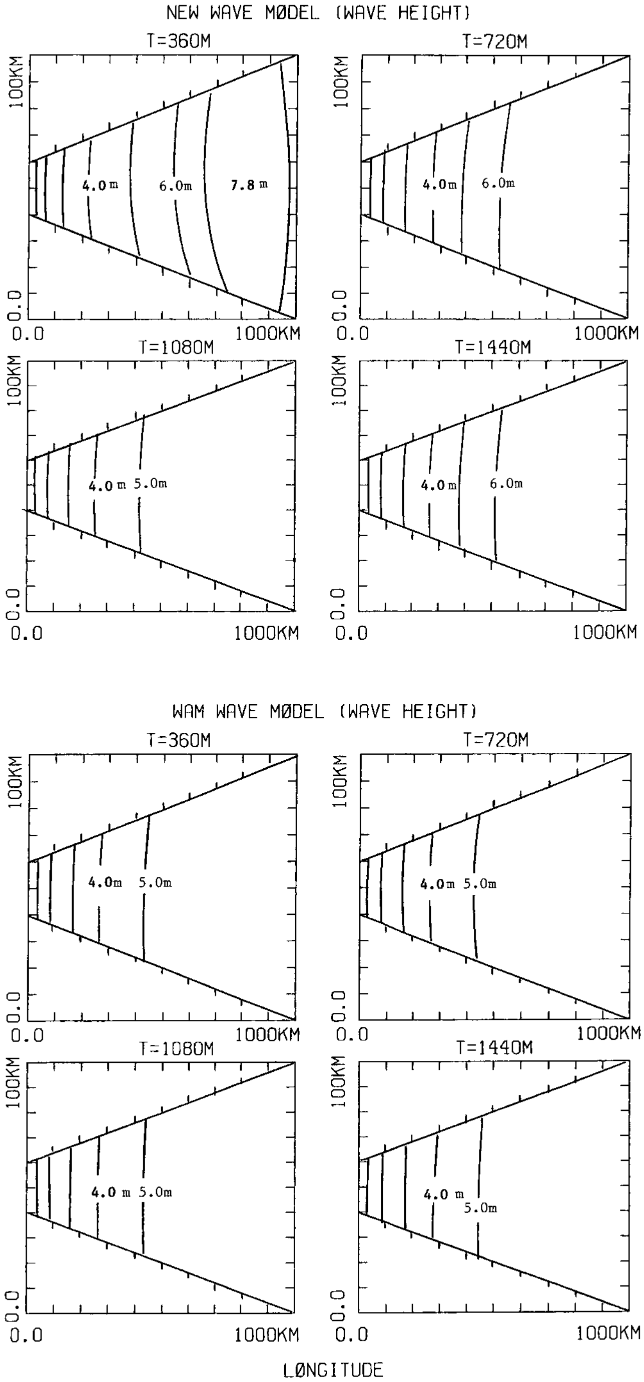

Figure 7. As in Figure 6, except the wind is oriented along the river from downstream to upstream: (a) from NCWM and (b) from WAM model. Units are in m.

significant thermocline and tide, it is impossible for seamount-trapped waves to be observed on the sea surface. Further discussion is presented by Lin and Chubb (submitted manuscript, 2001).

[34] The differences in sea state forecasting in a tidal estuary between these two models, NCWM and WAM, are significant. Seamount-trapped waves cannot be described by the WAM formulation, because it lacks the essential wave–current interaction terms. Model differences result from rapidly changing depths and unsteady currents, associated with the tidal estuary, which are important in the $\partial(c_\omega A)/\partial\omega$ term in the formulation of NCWM (2). This was mentioned in the discussion comparing NCWM and (3), the formulation for WAM. The other major reason that causes NCWM to differ from WAM is nonlinear dispersion. In high wave conditions, when water depth is shallow and currents are strong, nonlinear dispersion becomes very important. In our model, our breaking condition is that the waves break when $kd \geq 0.3$. Wave energy exceeding this limit is set to zero. In reality the nonlinearity should be stronger, and the difference between the two models' results

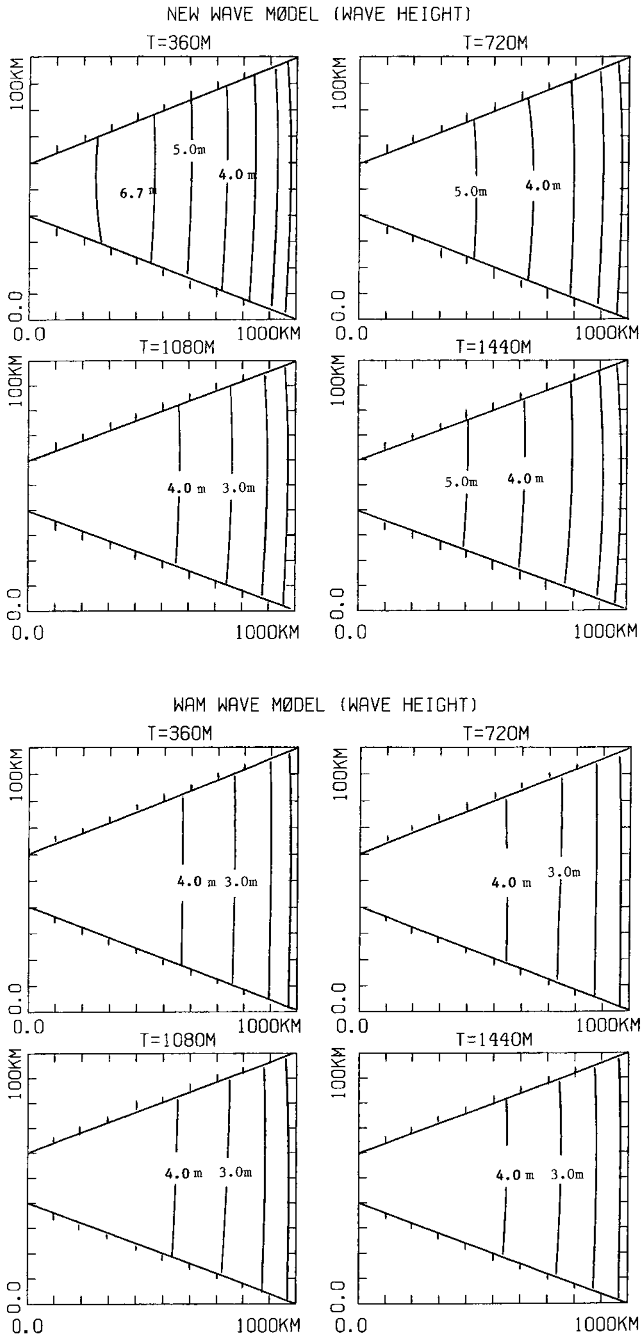

Figure 8. As in Figure 6, except the wind is oriented along the river from upstream to downstream: (a) from NCWM and (b) from WAM model. Units are in m.

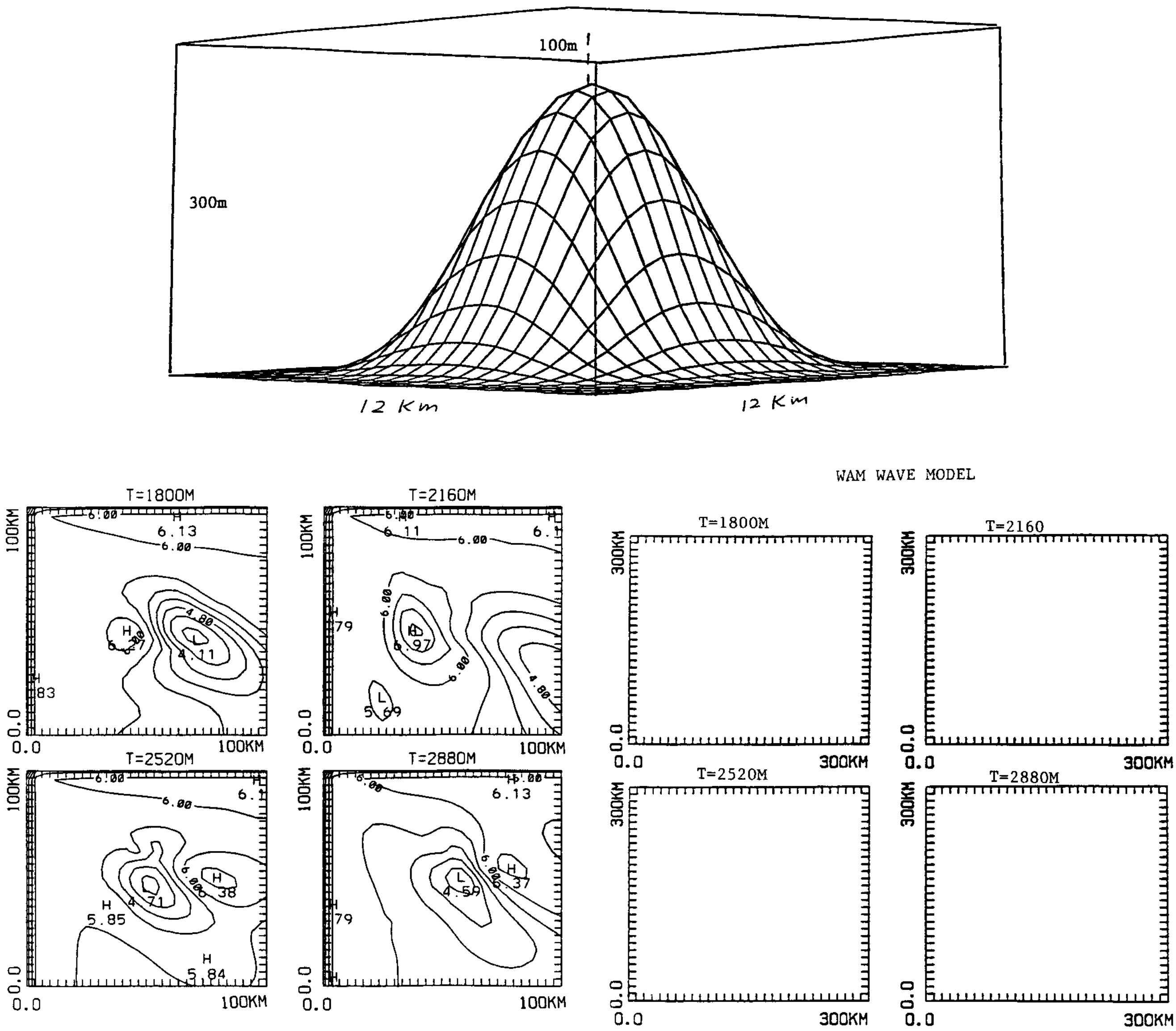

Figure 9. As in Figure 6, except no wind, with (a) ideal bottom seamount near the river month, (b) isolines for significant wave height as a function of time in minutes by NCWM, (c) isolines from WAM model, (d) density perturbation at 500 m depth (adapted from the study of *Beckmann and Haidvogel* [1997] (the solid circles are the mooring sites from the study of *Brink* [1995]), and (e) Synthetic Aperture Radar (SAR) image showing surface manifestation of seamount in northwest Pacific Ocean [*Etkin et al.*, 1991].

should be even greater. The nonlinear dispersion causes significant differences in the NCWM and WAM models' estimates for the group velocity, phase velocity and nonlinear wave–wave interactions, ultimately affecting estimates in sea state and wave height.

[35] It should be noted that the main differences between NCWM and WAM result from the physical terms, specifically wave–current interactions, unsteady current effect, and nonlinear dissipation. These terms are included in NCWM, but excluded from WAM. Furthermore, NCWM uses a high-quality stable numerical computational scheme, the well-known third-order Runge–Kutta method [*Gerald*, 1977]. By comparison, WAM uses the Euler scheme, which is a computationally unstable, and has numerical dispersion and dissipation, as discussed in section 3.1. Thus, we were able to show that NCWM's results agree well with the well-known observed seamount-trapped waves over Fieberling Guyot and a set of two seamounts in NE Pacific ocean, whereas WAM does not show these phenomena. This corroborates a recent study of Singapore Harbor showing that the agreement of NCWM to observational data was much better than that of WAM [*Lin and Silver*, 2000].

6. Conclusions

[36] For a tidal estuary, as considered in this study, currents and depth changes are the norm rather than the

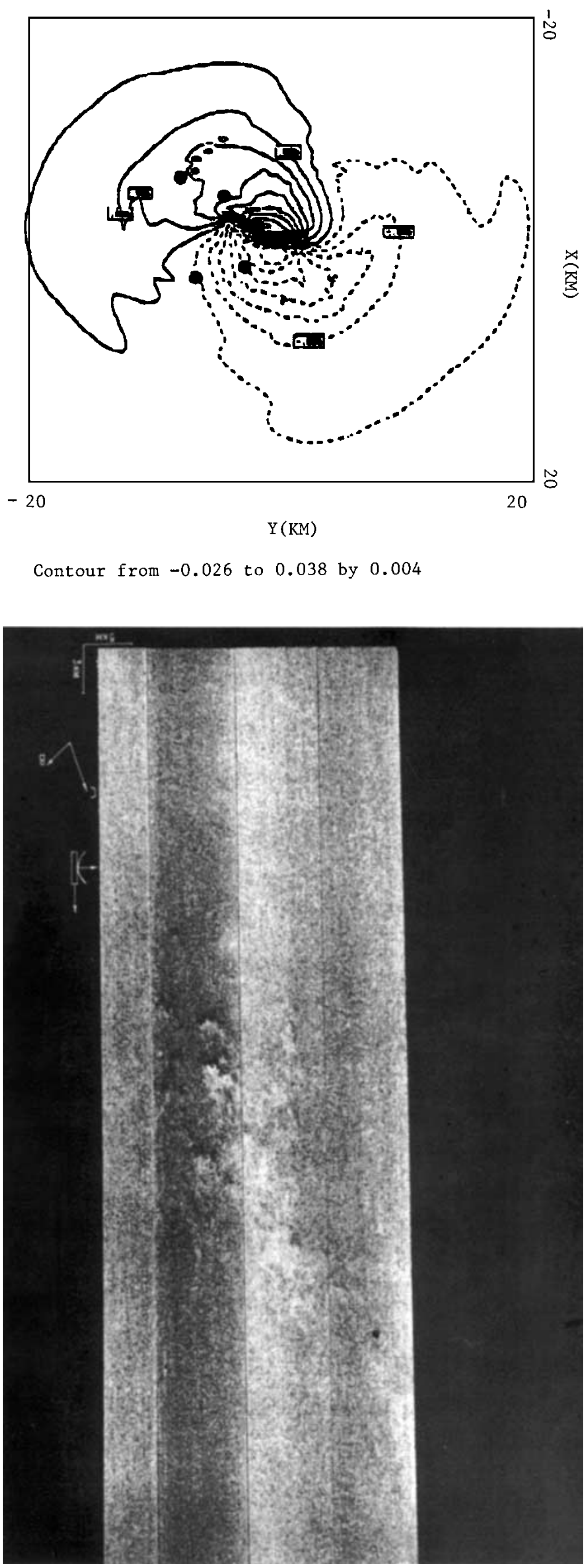

Figure 9. (continued)

exception. Therefore, any model used to simulate sea state should be able to simulate ambient currents and depth changes. Our new wave–current interaction model, NCWM, has action conservation as its basis and can readily simulate the dispersion effects due to unsteady currents and bottom topography. For example, the H_s cycles in Figures 6, 7, 8, and 9 result from action conservation and nonlinear dispersion in the NCWM formulation, as typified by $\partial(c_\omega A)/\partial\omega$ as well as the nonlinear effects of the action flux terms, $A\frac{\partial c_{g\lambda}}{\partial\lambda}$, $A\frac{\partial(c_{g\phi}\cos\phi)}{\partial\phi}$, and $A\frac{\partial c_{g\theta}}{\partial\theta}$. These terms do not appear in the WAM formulation and they actually can be neglected for large-scale motions in deep water without varying currents. However, in varying currents and shallow water, these effects can be important. Therefore, the WAM formulation shows no effect for topography or varying currents, no H_s cycles, no swell contours.

[37] Differences between the WAM wave model and NCWM, for example, the H_s cycles following the tidal variation in space and time, result from NCWM's ability to simulate wave–current interactions. This is especially evident when there are steady or unsteady currents, with rough bottom topography and finite depth water, typical of a tidal estuary. Associated effects are sea surface wave features reflecting the seamount-trapped waves, for example as presented in the discussion of Fieberling Guyot and as shown in SAR image over small seamounts near 51°N and 164°E in the northwest Pacific Ocean.

[38] This ability is not present in WAM. For example, for a flat bottom finite depth ocean, WAM computationally annihilates energy due to numerical dispersion and the dissipation, whereas NCWM is largely conservative because of its SOSI or third-order Runge–Kutta propagation schemes. Comparison with analytic results of simpler cases (as given decades ago by *Phillips* [1977]) further suggests that NCWM represents the kinematics more realistically than WAM. For strong unsteady tidal currents and depths, nonlinear dispersion and the action flux terms such as $\partial(c_\omega A)/\partial\omega$ cannot be neglected. Moreover, it is difficult to quantitatively estimate the relative importance of these effects. For example, the effect of first turning off nonlinear dispersion and then turning off the action flux terms is not equal to the sum of having both terms turned on. This is because of the nonlinear relations between nonlinear dispersion and the action flux terms.

[39] **Acknowledgments.** This wave–current study was funded by the Coast Guard (Canada) Search and Rescue New Initiatives Fund (SAR-NIF). The wave modeling program at BIO is funded by the Federal Panel on Energy Research and Development (Canada) under project 534201.

References

Bretherton, F. P., and C. J. R. Garrett, Wave trains in inhomogeneous moving media, *Proc. R. Soc. London, Ser. A*, *302*, 529–554, 1968.
Beckmann, A., and D. Haidvogel, A numerical simulation of flow at Fieberling Guyot, *J. Phys. Oceanogr.*, *102*, 5595–5613, 1997.
Brink, K. H., The effect of stratification on seamount-trapped waves, *Deep Sea Res., Part I*, *36*, 825–844, 1989.
Brink, K. H., On the generation of seamount trapped waves, *Deep Sea Res., Part I*, *37*, 1569–1582, 1990.
Brink, K. H., Tidal and lower frequency currents above Fieberling Guyot, *J. Geophys. Res.*, *100*, 10,817–10,832, 1995.
Chapman, D. C., Enhanced subinertial diurnal tides over isolated topographic features, *Deep Sea Res.*, *36*, 815–824, 1988.
Chapman, D. C., and D. B. Haivogel, Generation of internal lee waves trapped over a tall isolated seamount, *Geophys. Astrophys. Fluid Dyn.*, *69*, 31–65, 1993.

Chelomei, V. N., G. A. Efremof, K. Tz. Litovchenko, L. B. Neronsky, P. O. Salganik, S. S. Semenov, A. V. Smirrnov, and V. S. Etkin, Studies of the sea surface using the Kosmos-1870 high-resolution radar, *Issled. Zemli Kosm.*, vol. 8, pp. 80–90 and 306–321, in Russian, March–April 1990.

Dowd, M., P. W. Vachon, F. W. Dobson, and R. B. Olsen, Ocean wave extraction from RADARSAT synthetic aperture inter-look image cross-spectra, *IEEE J.*, in press, 2001.

Etkin, V. S., et al., Radiohydrophysical aerospace research of ocean, 83 pp., Acad. of Sci. USSR, Space Res. Inst. Publ. 1749, 1991.

Gerald, C. F., *Applied Numerical Analysis*, p. 516, Addison-Wesley-Longman, Reading, Mass., 1977.

Haidvogel, D., and A. Beckmann, *Numerical Ocean Circulation Modeling*, 318 pp., Imperial Coll. Press, London, 1999.

Hasselmann, K., et al., Measurements of wind-wave growth and swell decay during the Joint North Sea Wave Project (JONSWAP), *Dtsch. Hydrogr. Z., Erganz.heft, A*, *8*, 1973.

Hasselmann, K., R. K. Raney, W. J. Plant, W. Alpers, R. A. Shuchman, D. R. Lyzenga, C. L. Rufenach, and M. J. Tucker, Theory of synthetic aperture radar ocean imaging, *J. Geophys. Res.*, *90*, 4659–4686, 1985.

Huang, N. E., L. F. Bliven, S. R. Long, and C. C. Tung, An analytic model for oceanic whitecap coverage, *J. Phys. Oceanogr.*, *16*, 1597–1604, 1986.

Infeld, E., and G. Rowlands, *Nonlinear Waves, Solitons and Chaos*, 423 pp., Cambridge Univ. Press, New York, 1990.

Komen, G. J., L. Cavaleri, M. Donelan, K. Hasselmann, and P. A. E. M. Janssen, *Dynamics and Modelling of Ocean Waves*, 512 pp., Cambridge Univ. Press, New York, 1994.

Krogstad, H. E., O. Samset, and P. W. Vachon, Generalizations on the nonlinear ocean SAR transform and simplified SAR inversion algorithm, *Atmos. Ocean*, *32*, 61–82, 1994.

Lin, R. Q., Reply to comments on Part 1 by Tolman et al., *J. Phys. Oceanogr.*, *28*, 1291–1304, 1998a.

Lin, R. Q., Reply to Comments on Part II by Tolman et al., *J. Phys. Oceanogr.*, *28*, 1309–1318, 1998b.

Lin, R. Q., and N. H. Huang, The Goddard Coastal Wave Model, part 1, Numerical method, *J. Phys. Oceanogr.*, *26*, 833–847, 1996a.

Lin, R. Q., and N. E. Huang, The Goddard Coastal Wave Model, part 2, Kinematics, *J. Phys. Oceanogr.*, *26*, 848–862, 1996b.

Lin, R. Q., and W. Perrie, Nonlinear wave-wave interactions in finite water, *J. Geophys. Res.*, *104*, 11,193–11,213, 1999.

Lin, R. Q., and A. Silver, A study of Singapore Harbor-Changi Airport wave climatology as determined by a New Coastal Wave Model, Hydromechanics Dir. Rep. NSWCCD-50-TR-2000/015 (David Talor Model Basin), March 2000.

McLean, J. W., Instabilities of finite-amplitude water waves, *J. Fluid Mech.*, *114*, 315–330, 1982.

Pedlosky, J., *Geophysical Fluid Dynamics*, 624 pp., Springer-Verlag, New York, 1979.

Phillips, O. M., *The Dynamics of Upper Ocean*, second edition, 235 pp., Cambridge Univ. Press, New York, 1977.

Whitham, G. B., *Linear and Nonlinear Waves*, 628 pp., John Wiley, New York, 1974.

Yuen, H. C., and B. M. Lake, Nonlinear dynamics of deep water gravity waves, *Adv. Appl. Mech.*, *22*, 67–229, 1982.

R. Q. Lin, Department of Seakeeping, David Taylor Model Basin, Carderock Division, Naval Surface Weapons Center (NSWC), 9500 MacArthur Boulevard, West Bethesda, MD 20817-5700, USA. (LinRQ@nswccd.navy.mil)

W. Perrie, Ocean Sciences Division, Maritime Region, Fisheries and Oceans Canada, Bedford Institute of Oceanography, Dartmouth, Nova Scotia, Canada, B2Y 4A2.